Available online at www.sciencedirect.com

ScienceDirect

journal homepage: www.elsevier.com/locate/he

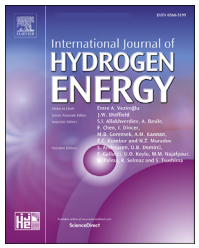

Room temperature hydrogen absorption by Mg and Mg–TiFe nanocomposites processed by high-energy ball milling

R.A. Silva [a], R.M. Leal Neto [b], D.R. Leiva [a,*], T.T. Ishikawa [a], C.S. Kiminami [a], A.M. Jorge Jr. [a], W.J. Botta [a]

[a] Departamento de Engenharia de Materiais, Universidade Federal de São Carlos, Rodovia Washington Luiz, km 235, CEP 13565 – 905, São Carlos, SP, Brazil

[b] Instituto de Pesquisas Energéticas e Nucleares (IPEN), Av. Lineu Prestes 2242, Cidade Universitária, CEP: 05508-000, São Paulo, SP, Brazil

ARTICLE INFO

Article history:
Received 22 January 2018
Received in revised form
17 April 2018
Accepted 24 April 2018
Available online 29 May 2018

Keywords:
High-energy ball milling
MgH_2
TiFe
Hydrogen absorption

ABSTRACT

Mg - 40 wt % TiFe nanocomposite was prepared by high-energy ball milling, HEBM, aiming improved hydrogen absorption at room temperature (RT). Four processing routes were chosen to separately investigate the effects of TiFe addition, HEBM processing and dispersion of TiFe particles, being: Route 1 – mechanical mixture of Mg and TiFe powders; Route 2 – HEBM of Mg + TiFe at 400 rpm for 12 h; Route 3 – HEBM of pure Mg at 400 rpm for 12 h to be used as reference; and Route 4 – HEBM of Mg + TiFe at 600 rpm for 36 h. In this case, TiFe was previously milled with ethanol to improve its refinement level. It is shown that the synergetic effects of TiFe addition, HEBM processing and thermal activation – involving the creation of Mg–TiFe interfaces, the refinement and distribution of TiFe and also the presence of free Fe – lead to good hydrogenation kinetics at RT in Mg–TiFe nanocomposite. It is also shown for the first time that the milled pure Mg can absorb hydrogen at RT.

Introduction

Hydrogen is a renewable and economically sustainable energy resource. It has been considered as a clean energy carrier, without toxic emissions [1–3]. Aside from conventional applications of hydrogen as in the synthesis of ammonia and methanol, and in the petrochemical industry, due to its high efficiency in generating power, it could be used as future fuel for electric vehicles and power generators as fuel cells. The noticeable advantage of using hydrogen in such applications is an absence of pollution because the only by-product is the water [3–5].

However, the hydrogen applications mentioned above face two crucial issues. Firstly, so far, hydrogen is mainly generated from fossil fuels [6], creating massive volumes of carbon dioxide, which is a notorious greenhouse gas, consequently affecting worldwide warm up and producing the nowadays noticeable clime variations. Furthermore, besides non-renewable, fossil fuels makes the world economically dependent on few geographical areas and large conglomerates.

* Corresponding author.
E-mail address: daniel.leiva@ufscar.br (D.R. Leiva).

https://doi.org/10.1016/j.ijhydene.2018.04.174
0360-3199/

Secondly, deployment of an economical, safe and uncomplicated storage method is an essential condition to promote the broader application of H_2 as an energy carrier [7,8]. Traditional methods of storing hydrogen included high-pressure gas cylinders and liquefied hydrogen, which are limited by technological issues as appropriate pressure vessels for compressing hydrogen gas and cryogenic temperatures respectively, beside large sizes and weights [9].

For the sake of solving the first above issue, the production of hydrogen imperatively needs to be substituted by clean and renewable feedstocks [4]. If one thinks about the primitive carbon cycle (without the use of fossil fuels), biomass is being identified as a promising renewable source. By using biomass, the world will be less dependent on fossil fuels and be contributing to a carbon dioxide neutral energy supply [10]. Among several alternatives reported in the literature, one may identify the exciting hydrogen production from steam reforming of vegetable oil, which comprises all referred striking consequences of biomass usage [see, for instance [3], and references therein].

Regarding the hydrogen storage issue, amid other solutions presented in the literature [11–17] the solid-state hydrogen storage using metal hydrides is an attractive strategy to overcome the limitations of gaseous and liquid alternatives [18,19]. Amidst all reversible hydrides for hydrogen storage, MgH_2 has the highest energy density (9 MJ/kg of Mg), along with high hydrogen gravimetric (7.6 wt %) and volumetric (6.5 H atoms. cm^{-3}) capacities. Besides, magnesium is a low-cost material and has a low specific weight, 1.45 g cm^{-3}, being the eighth most abundant element in the earth's crust [18].

The development of hydrogen storage materials, however, is currently impaired to two main different problems: (i) materials may have an appropriate hydrogen absorption/desorption temperatures near room conditions but with low storage capacity, and (ii) they may have high volumetric or gravimetric storage capacities but at very high desorption temperatures. In the case of magnesium, its practical application is linked with the last issue, i. e, the desorption temperature is in a range of 300–400 °C [19] with relatively low kinetics of hydrogen absorption/desorption [18].

Hydrides are not easily formed by merely exposing the metallic surface to hydrogen at RT, since there is usually a layer of oxide or hydroxide on the surface, preventing its direct contact with the gas. In the case of magnesium, the system must be heated at relatively elevated temperatures (at least 300 °C) to ensure fast reaction [20]. Two factors are responsible for this behavior. Firstly, the hydrogen gas must have access to the pure metallic magnesium to allow the reaction. As long as the magnesium oxide (or hydroxide) prevents such access, once the thermal expansion coefficients of the surface contaminants and the metal are different, the system must be heated to break this layer, thus exposing the metal to the hydrogen. Secondly, absorption kinetics is very slow at temperatures below 300 °C to generate hydrides within reasonable timescales [21].

It is well known that the formation of MgH_2 ceases after the establishment of a very thin layer of hydride on the metal surface [22]. This behavior has been correlated with a very slow (virtually none) diffusion of hydrogen through the hydride. Therefore, for the complete hydride formation, the starting metal must be of tiny geometric dimensions, i.e., either in particulate form, thin slices or films. Nevertheless, even with favorable geometric conditions, hydriding is supposed not to occur at RT because of the high activation energy for hydrogen gas dissociation. Exposure to oxygen only exacerbates the problem. Oxidized surfaces have higher activation energies for hydrogen gas dissociation than clean (activated) surfaces [23].

Lower desorption temperatures (<300 °C) has been reported for nanocrystalline MgH_2 obtained by ball milling [24], severe plastic deformation techniques (e.g., equal-channel angular pressing) [25–27], and through the addition of various catalysts [28]. Despite the advances produced by such techniques, especially in improving the desorption kinetics, temperatures of hydrogen desorption are considered still high, at least by the standards of the US DOE [29] which established as the ultimate goal a temperature range for hydrogen release from −40 to 85 °C.

Intermetallic compounds of transition metals are among several catalyst materials to assist the hydrogenation of the magnesium metal or destabilization of the magnesium hydride. In this case, the strategy of using composites is based on the mixture of dissimilar materials, exploiting the best characteristics of each component. It has been reported in the literature [30–32] the combination of TiFe, which absorbs and desorbs hydrogen at or near RT, with Mg, which has higher storage capacity than TiFe. HEBM has been used to produce the composites by mechanical alloying, usually starting from powders of Mg and TiFe in variable proportions. In these investigations, besides stoichiometric TiFe compound, $Ti_{1.2}Fe$ [30] and TiFeMn [31,32] powders were alternatively mixed with Mg powder. The best-reported result was achieved by Kondo et al. [32]. The authors have milled Mg and $TiFe_{0.92}Mn_{0.08}$ (50/50 wt%) in a planetary ball mill (Fritsch, Pulverisette 7), with some n-hexane, at 600 rpm for 80 h. After a lengthy heat treatment, the composite absorbed ~3.3 wt% of hydrogen at ~25 °C (1.55 MPa) for 20 h. Desorption started at 300 °C under a hydrogen pressure of 0.1 MPa.

In other studies, nanometric nickel [33] or multi-walled carbon nanotubes (MWCNTs) [34] were added to the MgH_2 + TiFe composites. The authors obtained good capacities (higher than 4.5 wt % of H_2) but at higher absorption/desorption temperatures (above 267 °C). Chen et al. [35] have also used CNTs but on Mg + 30 wt % TiFe composites. Astonishing capacity was obtained (6.6 wt %) at 150 °C after just 1 min. These results have emphasized the crucial role of a high dispersion grade of TiFe particles (nanoparticle dispersion) for the absorption/desorption properties and the necessity of activating the composite by heat treatment cycling.

In a previous work [36], we have performed HEBM of MgH_2+40 wt % TiFe using a planetary and a shaker mill. After dehydriding the as milled composites under vacuum at 350 °C, samples were cooled to perform kinetics measurements at RT. The best hydrogen kinetics (3 wt % at the first hour) was attained by the composite sample prepared in the planetary mill for 36 h. Higher hydrogen capacity (4.0 wt %) was observed - for the specimen milled in the shaker mill for 2 h - but only after 13 h of exposure to hydrogen.

In this paper, the combination of TiFe with metallic Mg by HEBM to produce Mg - 40 wt % TiFe nanocomposites is reported. An evaluation of the catalytic effect of TiFe on the hydrogen absorption properties was performed at RT. The desorption properties were determined by thermal analyses after hydrogen absorption.

Experimental

The TiFe intermetallic compound was synthesized by HEBM of powders of TiH_2 and Fe, followed by heating under vacuum as described elsewhere [37]. A very fine Mg powder was achieved by milling of commercial MgH_2 under a hydrogen pressure of 10 bar, followed by desorption at 350 °C and heating to 430 °C under vacuum, and was used as raw material to produce the Mg–TiFe nanocomposites by HEBM, as detailed in Table 1.

Mixing and ball milling of the powders were performed in a Fritsch Planetary Mill Pulverisette 6. The milling vial was loaded with 1 g of Mg added of 0.67 g of TiFe (40% of the total mass) and 66.8 g of steel balls (ball-to-powder weight ratio of 40:1). For route 1, a simple mixture of Mg and TiFe was performed in the above milling machine (for 1 h) using no milling balls Route 3 was accomplished to produce Mg powders to be used as a reference. All milling experiments were performed at RT.

As observed earlier [36,37], using the same milling conditions as in the present work, the authors did not find any significant iron contamination after milling. Therefore, it is expected that the composition will not change substantially for the same milling conditions used in this study. Thus, no chemical analysis was performed after milling. Therefore, the final composition was considered as being the nominal one (Mg – 40 wt % TiFe).

The comparison of results for the samples processed by the routes 1 and 2 were used for the investigation of effects of ball-milling and simple mixing. Routes 2 and 3, in which milling has similar parameters, are useful to investigate effects of the addition of TiFe on properties of hydrogen absorption/desorption, the process of thermal activation, and hydrogenation at RT.

The comparison between routes 2 and 4 highlights the effects of different procedures of milling on the composite microstructure and its effect upon the hydrogen absorption/desorption properties. A previous wet milling of TiFe in absolute grade ethanol for 24 h at 400 rpm was applied to optimize the refinement and to improve the distribution of TiFe in route 4. All studied materials were stored and handled inside an MBraun glove box under argon atmosphere, with oxygen and moisture levels below 0.1 ppm.

Table 1 – Details of the processing routes for pure Mg and Mg–TiFe nanocomposite, ball-to-powder weight ratio was 40:1 for all conditions.

Route	Mg (wt. %)	TiFe (wt. %)	Description
Route 1	60	40	Mixture for 1 h at 400 rpm
Route 2	60	40	HEBM for 12 h at 400 rpm
Route 3	100	0	HEBM for 12 h at 400 rpm
[a]Route 4	60	40	HEBM for 36 h at 600 rpm

[a] Previous wet milling of TiFe using ethanol.

The present phases were characterized by X-ray diffraction (XRD) in a Siemens D 5005 diffractometer using monochromatic Cu-K_α ($\lambda = 1.5418$ Å). Bragg angles ranged from 20° to 90°, using a step-scan of 0.032° and a count time of 1 s. After removing the $K_{\alpha 2}$ radiation and instrumental broadening, the crystallite sizes of Mg, TiFe and MgH_2 were estimated from single-line pseudo-Voigt analyses of the main reflections, in order to separate the effects of microstrain from those of crystallite size on broadening of peaks [38,39].

Hydrogen sorption properties were determined by a home-made volumetric Sievert-type apparatus using a sample mass of 150 mg. The samples were first exposed to 350 °C and 20 bar of H_2 (g) for 1 h, desorbed at 350 °C (from 1 bar of H_2) and subsequently heated to 430 °C under continuous vacuum. After this activation step, experiments of hydrogen absorption were performed at RT under 20 bar of H_2 (g). In the case of route 3, the full activation of Mg was obtained after several cycles of absorption/desorption at 350 °C.

Hydrogen desorption behavior was investigated by simultaneous differential scanning calorimetry–thermogravimetry–STA (TGA-DSC) coupled to a quadrupole mass spectrometry (QMS) of the evolved gasses in a Netzsch STA 449C Jupiter + QMS 403C Aëolos apparatus, with a constant heating rate of 10 K/min under purified argon (25 ml/min). Samples of about 10 mg were used.

Microstructural characterization of the powders in the as-milled and hydrogenated conditions was performed by scanning electron microscopy (SEM) in a FEI Inspect S 50 operating at 25 KV and using only backscattered electrons (BSE) detector to emphasize the chemical contrast. Microstructural and structural analyses of wet-milled TiFe were also accomplished by transmission electron microscopy (TEM) in an FEI TECNAI G^2 F20 operating at 200 KV. The microscope was used in the conventional TEM mode and also in the scanning transmission electron microscopy (STEM) mode. Selected area electron diffraction (SAED) patterns were indexed using the JEMS software [40].

Results and discussion

Fig. 1 shows XRD patterns of the precursor materials. Only tetragonal MgH_2 is present in the un-milled condition (pattern a1) and after milling of MgH_2 for 24 h in an argon atmosphere (pattern a2). After milling of MgH_2 for 24 h in a hydrogen atmosphere (pattern a3), one can observe that the tetragonal MgH_2 is still present, but the orthorhombic MgH_2 starts forming. After desorption of MgH_2 milled in hydrogen, only the hcp-Mg is present (pattern a4).

Regarding TiFe, the XRD pattern indicated as a5 in Fig. 1 reveals the presence of the cubic TiFe. However, after wet milling of TiFe for 24 h under argon atmosphere (pattern a6), TiFe coexists with Fe and the TiC. Such a decomposition of TiFe is partially due to the interaction between the absolute grade ethanol and Ti, resulting in the formation of TiC and free Fe. The presence of Fe in the final compound is not a matter of concern since there is an association between the presence of

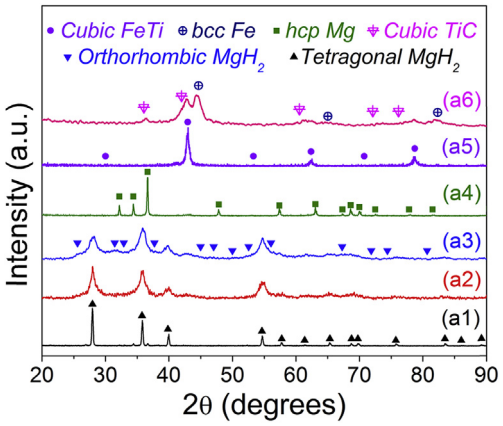

Fig. 1 – XRD patterns for the precursor materials in the following conditions: (a1) un-milled commercial MgH_2, (a2) MgH_2 after milling 24 h under argon, (a3) MgH_2 after milling 24 h under hydrogen, (a4) Mg from desorption of MgH_2 milled under hydrogen, (a5) as-synthesized TiFe and (a6) TiFe after wet milling 24 h under argon.

nanometric Fe and kinetic improvement [32,41], and also with the pinning of grain boundaries [42].

Fig. 1 also shows a large peak broadening after milling, indicating a significant crystallite size refinement for all materials. The un-milled commercial MgH_2 presented a crystallite size of ~72 nm. After milling of MgH_2 under argon atmosphere, there was a reduction of the crystallite size to ~22 nm. The milling of MgH_2 under a hydrogen atmosphere led to a more efficient refinement, with final value of ~9 nm. The average crystallite size of TiFe was reduced from ~32 nm to ~7 nm after wet milling in absolute grade ethanol.

Fig. 2 presents TEM/STEM information regarding TiFe after wet-milling. Fig. 2a shows a bright field (BF) TEM image of agglomerated particles, whose SAED pattern is shown in Fig. 2b. The indexing of this pattern, using the ICSD 100533 CIF file, reveals that this agglomerate is mainly formed by the cubic TiFe. Additionally, the ring-like SAED pattern demonstrates that TiFe particles are of very small sizes. In fact, one can observe in the Z-contrast image in Fig. 2c, obtained by a High Angular Annular Dark Filed (HAADF) detector from the same agglomerated particles in Fig. 2a, that TiFe particles are in the nanosize range. These observations confirm the comments regarding XRD patterns broadening.

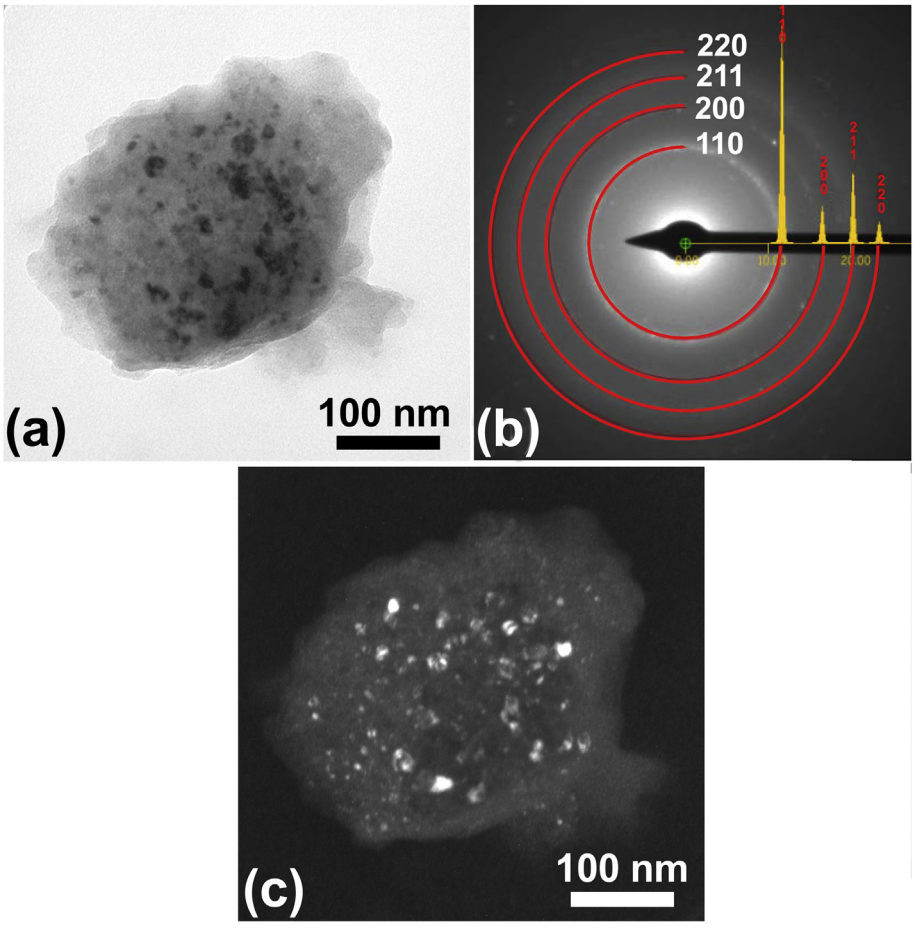

Fig. 2 – TEM observations of TiFe after wet milling for 24 h in absolute grade ethanol. (a) bright field (BF) TEM image of agglomerated particles. (b) Select area diffraction pattern (SAED) of the same region of Fig. 2a. (c) STEM image using a High Angular Annular Dark Field (HAADF).

Fig. 3 presents XRD patterns for the Mg + TiFe nanocomposite (route 2) from the milled condition to the final hydrogenated state. The identification of phases revealed the presence of Mg, TiFe and a small amount of Fe in the as-milled condition. After the activation procedure, Mg is entirely converted to MgH_2; TiFe is still present and the amount of Fe is increased, suggesting a decomposition of TiFe. After the first desorption, MgH_2 is totally reversed to the Mg; TiFe and Fe are still present. After the last absorption at RT, Mg is partially converted to MgH_2, which continues coexisting with TiFe and Fe. After the first decomposition during the activation procedure, TiFe and Fe are stabilized, with no further changes in their relative phase amounts.

Fig. 4 presents XRD patterns of the Mg–TiFe composite after processing by the different routes. In pattern c1, it is observed the presence of only Mg and TiFe after the simple mixing of both phases. In pattern c2, which corresponds to milling the mixture for 12 h at 400 rpm, it is observed that Fe starts to form, once again suggesting the decomposition of the TiFe. By milling Mg, following the route 3, pattern c3, besides the obvious presence of Mg, there is the formation of MgO, which, even expected to form during ball milling [19], was clearly observed only for this sample.

Finally, pattern c4, which corresponds to route 4, shows the expected presence of Mg and TiFe, together with the phases formed from the TiFe synthesis. In other words, decomposition of TiFe results in Fe and the TiC, as already discussed. In addition, one can also observe broadening of the peaks related to the decreasing of crystallite size. Table 2 presents information regarding such sizes.

BSE-SEM observations are shown in Fig. 5 highlighting the effects of the different routes on the morphology, distribution and particle size of TiFe. Fig. 5a shows that, after mixture (route 1), Mg and TiFe powders agglomerated in round-like particles whose size distribution is of multimodal characteristic. In addition, one can observe that TiFe is not well distributed in the Mg particles. Fig. 5b and d reveal the microstructure of nanocomposite after HEBM following routes 2 and 4, respectively. After processing by route 2 (Fig. 5b), the size of Mg particles agglomerate is reduced and keeps the round shape, but TiFe, even with a bimodal size distribution, is better distributed in Mg than after processing by route 1 (Fig. 5a). In the case of route 4 (Fig. 5d), after wet milling and further HEBM, particles have re-agglomerated. However, TiFe agglomerates are of smaller size and much better distributed than for route 2. Agglomeration was also observed for Mg after processing by route 3 (Fig. 5c). In this case, the agglomerates follow the same behavior as for route 4 (re-agglomeration), but with sizes following the same distribution behavior as for route 1. In addition, agglomerated particles are of very irregular shape.

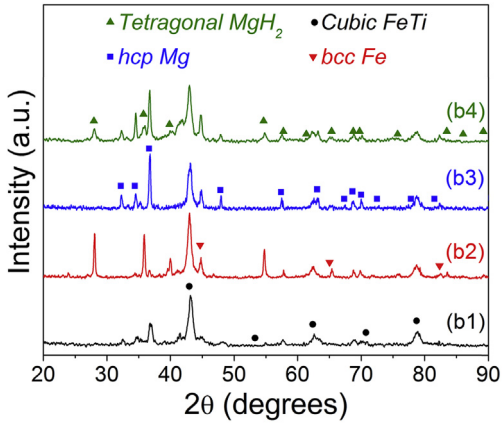

Fig. 3 – XRD patterns for the Mg + TiFe nanocomposite in the following conditions (route 2): (b1) after HEBM; (b2) after activation; (b3) after hydrogen desorption and (b4) after the final hydrogen absorption at RT.

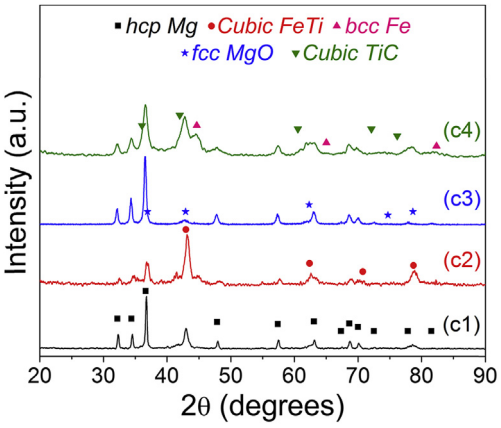

Fig. 4 – XRD patterns for the different processing routes detailed in Table 1, showing effects of HEBM and addition of TiFe on the nanocomposite material: (c1) route 1, (c2) route 2, (c3) route 3, and (c4) route 4.

Table 2 – Evaluation of crystallite size (t) of the nanocomposite.

Route	After processing t (nm)		After absorption of 15 h at RT t (nm)		
	Mg	TiFe	Mg	TiFe	MgH_2
Route 1	85	15	90	17	32
Route 2	26	14	47	14	17
Route 3	31	–	[a]59	–	[a]20
Route 4	18	7	–	6.5	15

[a] Absorption during 50 h.

Fig. 6 presents XRD patterns for the different processing routes (Fig. 4 and Table 1) after hydrogen absorption at RT. Characterization of these patterns shows that the phases analyzed in Fig. 4 continue to be present either in higher or smaller amounts. However, different routes produced different hydrides with dissimilar amounts. As one can observe, after hydrogen absorption, the simple mixing of Mg and TiFe (route 1 - pattern d1) produced only tetragonal MgH_2 and most of Mg is still present.

Subsequent to route 2 (milling of the nanocomposite for 12 h) and hydrogen absorption, pattern d2 exposes that there is a little increase of the amount of tetragonal MgH_2, and the fcc-$TiH_{1.92}$ starts to be formed. Pure Mg was processed by route 3 and further hydrogenated for 50 h. However, due to oxidation (Fig. 4), several cycles of thermal activation were necessary to accelerate the hydrogen absorption kinetics at RT.

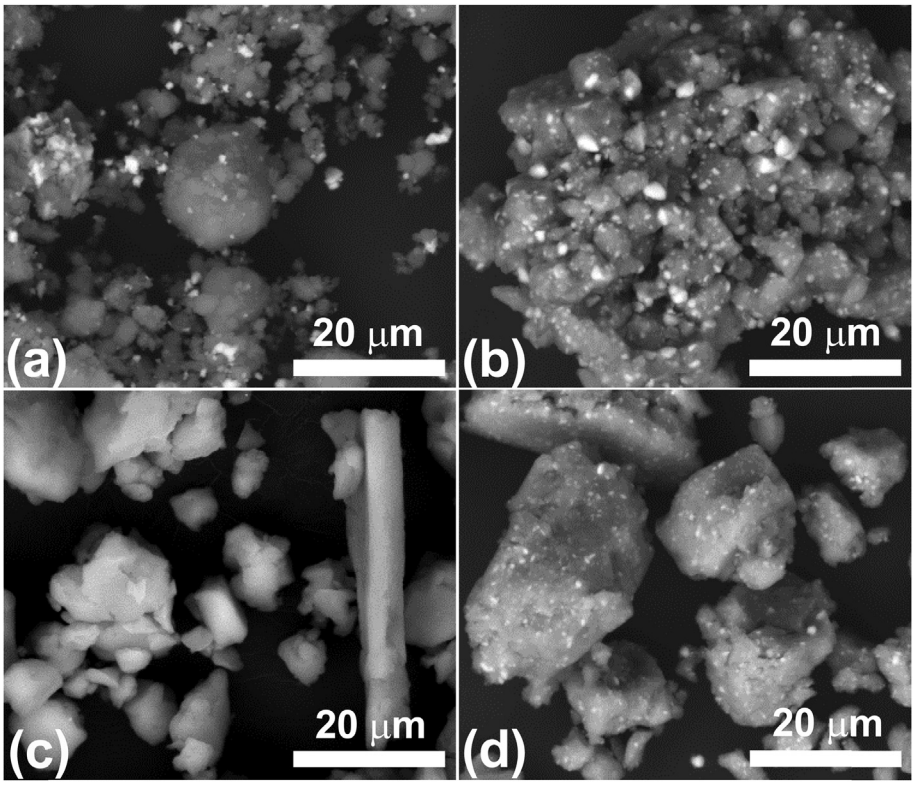

Fig. 5 – BSE-SEM images of nanocomposites produced through the different processing routes, as detailed in Table 1. (a) Route 1, (b) route 2, (c) milled Mg from route 3 and (d) route 4. White = particles of TiFe and Gray = matrix of Mg.

Obviously, this procedure almost doubled the crystallite size and, even so, MgO (pattern d3) is still present after hydrogenation and Mg was also partially converted into the MgH_2, in smaller amount than in the hydrogenated nanocomposite produced by route 2, and similarly to the one produced by simple mixing of Mg and TiFe.

However, it is worth emphasizing that the absorption occurred at RT, and according to the authors' knowledge, this is the first time that one reports hydrogen absorption by Mg at RT. Finally, route 4 produced the best results regarding amounts of absorbed hydrogen. This behavior can be seen in pattern d4 that shows increased amounts of MgH_2.

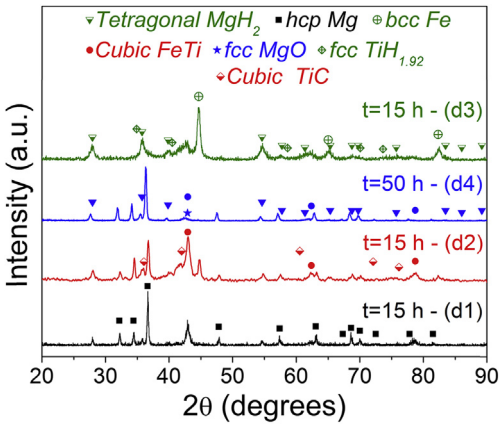

Fig. 6 – XRD patterns for the different processing routes (Fig. 4 and Table 1) after absorption at room temperature, using 20 bar of H_2, during the time = t, as indicated in the Figure. (d1) route 1, (d2) route 2, (d3) route 3 and (d4) route 4.

In fact, these results show an operative and synergetic catalytic effect of TiFe, associated with a small amount of Fe and reduction of crystallite size of those two phases and Mg, which decreases in the processing route sequence of 1, 2 and 4. In addition, also the effectiveness of the catalytic effect grows in the same sense, which may be linked as well with the reduced crystallite size of TiFe together with an increased amount of nanometric Fe. Further, Table 2 presents the crystallite sizes after hydrogen absorption at RT, compared to raw materials processed by the different routes (Table 1).

As one can observe, crystallite sizes of nanocomposite materials continue to be in the nanosize range after activation and hydrogenation. This fact may be due to the pinning effect produced by nanosized phases such as iron or even TiFe. The large change observed for route 3 is due to the absence of such pinning effect and, of course, due to the several cycles of activation.

Hydrogenation kinetics and hydrogen desorption properties are presented in Fig. 7, whose quantitative details are introduced in Tables 3 and 4. Fig. 7a shows the effects of HEBM and addition of TiFe, following the different routes (Table 1), on hydrogen absorption kinetics of the nanocomposite at RT, compared to pure Mg (route 3).

It is possible to confirm the synergetic effect of the TiFe and Fe catalytic presence and crystallite size as already discussed in the analysis of Fig. 6. In other words, the addition of TiFe has improved kinetics following the processing route

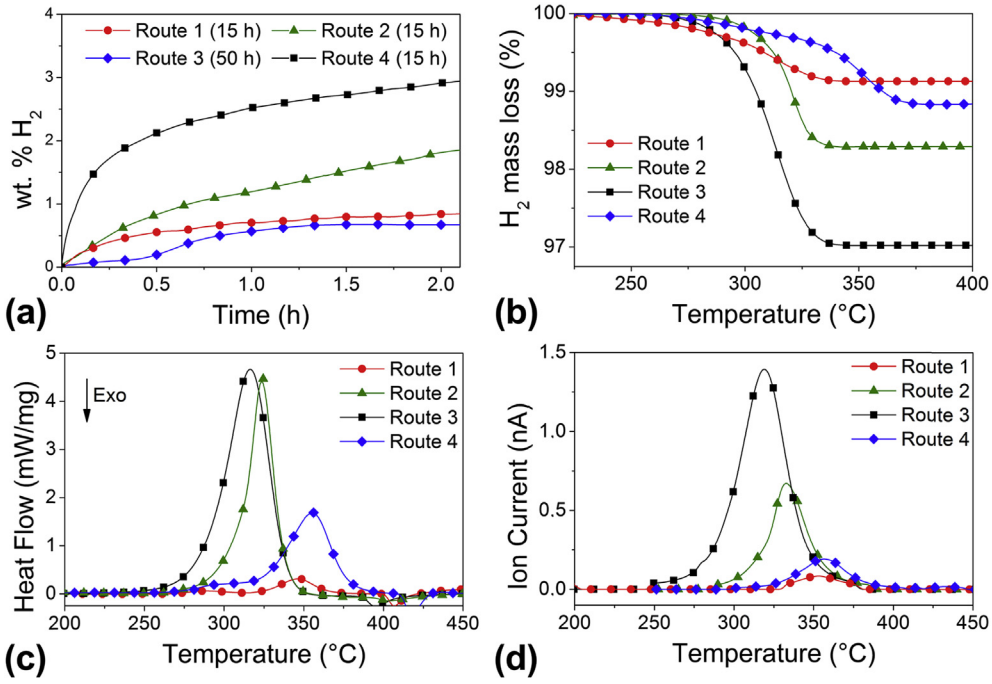

Fig. 7 – Hydrogenation kinetics and hydrogen desorption properties for all analyzed routes (a) first 2 h of room temperature absorption at 20 bar showing the kinetics of hydrogen absorption, (b) TGA, (c) DSC, (d) QMS.

sequence of 1, 2 and 4, which may be associated to the catalytic effect of TiFe linked as well with the reduced crystallite size of TiFe together with an increased amount of nanometric iron. In addition, if compared with pure Mg processed by route 3, the lower level of oxidation in nanocomposites, which was present in pure Mg, assisted the hydrogenation by avoiding incubation times. Such a beneficial effect of TiFe and free Fe in the hydrogenation kinetics of Mg was already reported in the literature [32,41,43].

From XRD analysis (Fig. 6) one can observe a high amount of un-transformed Mg to hydride from routes 1 and 2, respectively, after the activation process followed by hydrogenation for 15 h at RT. However, a very small amount of untransformed Mg was observed for route 4 after similar procedures of hydrogenation.

The influence of TiFe (and Fe) can also be observed in the hydrogen storage capacities, which reached a maximum of 3.94 wt % after processing following route 4 and further activation and hydrogenation at RT. This is a very attractive value considering earlier reports of the literature [30–35], and the comparatively less severe processing and/or hydrogenation conditions used here. On the other hand, a low amount of MgH_2 was transformed from Mg synthesized by route 3 after full activation (several cycles of absorption/desorption) and absorption of 50 h at RT. However, as stated above, absorption was at RT, which was never reported in the literature. Thus, the procedures used for processing and activation had an enormous influence on this behavior.

The above results are in agreement with the literature [41], which relates that the addition of TiFe improved the rate of hydrogen physisorption. Thermal activation of Mg/TiFe interfaces, during the activation process, makes the initial diffusion of physisorbed hydrogen faster during the absorption at RT. Thus, crystallite size, presence of catalysts and the activation process had an important role on hydrogen absorption kinetics. In the same sense, the better the refinement and homogenous spatial distribution of TiFe, the faster the kinetics of hydrogen absorption for the Mg at RT, which followed the processing route sequence of 1, 2 and 4.

TGA results presented in Fig. 7b, confirms the same effects observed for hydrogenation, i.e., Mg processed through different routes (Table 1) showed different desorption properties, repeating the same sequence of processing as for the absorption. For route 1, the content of desorbed hydrogen was smaller than 1 wt %. For route 3, the release of hydrogen reached a content of 1.17 wt % after full activation and

Table 3 – Summary of properties of dehydrogenation/hydrogenation performed in a Severt apparatus, after one cycle of thermal activation at 350 °C followed by absorption at room temperature and 20 bar.

Volumetric measurements (Sievert apparatus)			
Material	Condition	Absorption time (h)	wt. % H2
MgH_2	Commercial	20	[a]7.16
MgH_2	Milled under H_2 for 24 h	20	[a]6.32
Composite	Route 1	15	1.14
Composite	Route 2	15	2.88
Pure Mg	Route 3	50	0.85
Pure Mg	Route 3	100	–
Pure Mg	[b]Route 3	50	–
Composite	Route 4	15	3.94

[a] First desorption followed by absorption, both at 350 °C.
[b] Sample activated after several cycles of absorption/desorption at 350 °C.

Table 4 – Summary of properties of dehydrogenation/hydrogenation performed by calorimetric measurements, after one cycle of thermal activation at 350 °C followed by absorption at room temperature and 20 bar.

Calorimetric measurements (STA-449C)							
Material	Condition	Absorption time (h)	Temperature (°C)			Area (J/g)	TGA (%)
			Onset	Peak	End		
MgH_2	Commercial	20	435	444	462	1860	5.90
MgH_2	Milled in H_2/24 h	20	376	407	441	1735	6.60
Composite	Route 1	15	300	317	335	89	0.85
Composite	Route 2	15	309	323	338	617	1.70
Pure Mg	Route 3	50	317	364	393	61	0.60
Pure Mg	Route 3	100	326	376 and 415	423	113	0.93
Pure Mg	*Route 3	50	328	356	408	234	1.17
Composite	Route 4	15	287	317	339	997	2.95

*Sample activated after several cycles of absorption/desorption at 350 °C.

absorption of 50 h. Thus, milled Mg can absorb hydrogen at RT without additions of any catalyst. However, periods of hydrogenation to absorb contents of hydrogen higher than 1 wt % may be longer than 100 h, depending on procedures of milling and activation.

Fig. 7c and d presents desorption results obtained by DSC and QMS after processing of Mg through different routes (Table 1) and hydrogenation at RT. The exothermic peaks in Fig. 7c suggest the recrystallization of Mg after MgH_2 desorption. From Fig. 7c, it is also possible to observe that additions of catalyst and their distribution, and structural refinement are influencing the onset desorption temperature.

This influence is again following the same sense of processing routes and the consequent refinement and catalyst distribution. For instance, the onset desorption temperature dropped 148 °C from un-milled commercial MgH_2 to the MgH_2 obtained at RT from activated nanocomposite processed by route 4. The change of milling parameters from routes 2 to 4 did not lead to a significant difference in the onset desorption temperature, in spite of being better for route 4. Likewise, MgH_2, obtained from the hydrogenation of Mg processed by route 3 (without TiFe), had its peak temperature increased by 33–92 °C in comparison with the one for route 2 (with TiFe), therefore, reinforcing the effect of the activation process on the desorption behavior. Fig. 7d confirms the desorption behavior observed in Fig. 7c and, indirectly, also the ones observed in Fig. 7b regarding desorbed amounts. There are two small secondary peaks of dehydrogenation with onset near to 100 °C and near to 150 °C, respectively, for hydrogenated nanocomposites samples from routes 4 and 1, which may be related to the release of adsorbed hydrogen on the sample surface.

From the above results and discussions it is possible to observe that refinement of particles of MgH_2 and TiFe, catalytic effects of TiFe and small amounts Fe have had an important role in the decrease of desorption temperatures of MgH_2 (Tables 2 and 3).

Conclusions

It was shown that activated pure Mg obtained from desorption of milled MgH_2 can absorb hydrogen contents higher than 1 wt % at RT, depending on milling and activation parameters. The synergetic effects of addition of TiFe and small amounts of nanostructured Fe, high-energy ball milling and thermal activation led to important improvements of the hydrogen absorption kinetics of Mg at RT. For example, the activated nanocomposite produced by ball milling with addition of wet-milled TiFe reached the hydrogen storage capacity of 3.94 wt %, after absorption for 15 h at RT. It is clear that the refinement of TiFe and its homogeneous distribution in the matrix of Mg were essential for improving properties of hydrogen absorption at RT. The hydrogen desorption temperature range was considerably reduced in the Mg–TiFe nanocomposites in comparison with commercial or milled MgH_2.

Acknowledgements

The authors would like to thank the Brazilian institutions CNPq and CAPES for the financial support, and to the Laboratory of Structural Characterization of the Federal University of São Carlos (LCE/DEMa/UFSCar) for the use of electron microscopy facilities. The authors D. R. Leiva, T. T. Ishikawa, C. S. Kiminami, A. M. Jorge Jr and W. J. Botta are grateful for the funding by FAPESP (grant number 2013/05987-8).

REFERENCES

[1] Kapdan IK, Kargi F. Bio-hydrogen production from waste materials. Enzym Microb Technol 2006;38:569–82.
[2] Hosseini SE, Wahid MA. Hydrogen production from renewable and sustainable energy resources: promising green energy Carrier for clean development. Renew Sustain Energy Rev 2016;57:850–66.
[3] Tao K, Arano H, Zhang P, Ai P, Han L, Tsubaki N. Enhanced hydrogen production from steam reforming of vegetable oil over bimodal ZrO_2-SiO_2 supported Ni catalyst. Chemistry Select 2017;2:527–32.
[4] Ni M, Leung DYC, Leung MKH. A review on reforming bio-ethanol for hydrogen production. Int J Hydrogen Energy 2007;32:3238–47.
[5] Wang Y, Deng W, Liu X, Wang X. Electrochemical hydrogen storage properties of ball milled multi-wall carbon nanotubes. Int J Hydrogen Energy 2009;43:1437–43.

[6] Hu X, Lu G. Investigation of steam reforming of acetic acid to hydrogen over Ni–Co metal catalyst. J Mol Catal A 2007;261:43–8.
[7] Ozarslan A. Large-scale hydrogen energy storage in salt caverns. Int J Hydrogen Energy 2012;37:14265–77.
[8] Saxena S. Hydrogen production by chemically reacting species. Int J Hydrogen Energy 2003;28:49–53.
[9] Züttel A, Remhof A, Borgschulte A, Friedrichs O. Hydrogen: the future energy Carrier. Phil Trans R Soc A 2010;368:3329–34.
[10] Zhang B, Tang X, Li Y, Xu Y, Shen W. Hydrogen production from steam reforming of ethanol and glycerol over ceria-supported metal catalysts. Int J Hydrogen Energy 2007;32:2367–73.
[11] Mishra A, Banerjee S, Mohapatra SK, Graeve QA, Misr M. Synthesis of carbon nanotube–TiO2 nanotubular material for reversible hydrogen storage. Nanotechnology 2008;19:445607–14.
[12] Zeng K, Zhang D. Recent progress in alkaline water electrolysis for hydrogen production and applications. Energy Combust Sci 2010;36:307–26.
[13] Frackowiak E, Beguin F. Electrochemical storage of energy in carbon nanotubes and nanostructured carbons. Carbon 2002;40:1775–87.
[14] Fang B, Zhou H, Honma I. Ordered porous carbon with tailored pore size for electrochemical hydrogen storage application. J Phys Chem B 2006;110:4875–80.
[15] Li S, Pan W, Mao Z. A comparative study of the electrochemical hydrogen storage properties of activated carbon and well-aligned carbon nanotubes mixed with copper. Int J Hydrogen Energy 2005;30:643–8.
[16] Strobel R, Garche J, Moseley PT, Jorissen L. Hydrogen storage by carbon materials. J Power Sources 2006;159:781–801.
[17] Lueking AS, Pan L, Narayanan DL. Effect of expanded graphite lattice in exfoliated graphite nanofibers on hydrogen storage. J Phys Chem B 2005;109:12710–7.
[18] Sakintuna B, Lamari-Darkrim F, Hirscher M. Metal hydride materials for solid hydrogen storage. Int J Hydrogen Energy 2007;32(9):1121–40.
[19] Varin RA, Czujko T, Wronski ZS. Nanomaterials for solid state hydrogen storage. New York: Springer; 2009.
[20] Vigeholm B, Kjøller J, Larsen B, Pedersen AS. Formation and decomposition of magnesium hydride. J. Less Common Met 1983;89:135–44.
[21] Pedersen AS. Magnesium (beryllium) and alkaline earth (calcium, strontium and barium) hydrides. Diffus. Defect Data. Solid State Data B. Solid State Phenom 1996;49/50:35–70.
[22] Pedersen AS, Jensen K, Larsen B, Vigeholm B. The formation of hydride in pure magnesium foils. J. Less Common Met 1987;131(1–2):31–40.
[23] Andreasen A. Predicting formation enthalpies of metal hydrides. Risø-R-1484. 2004.
[24] Huot J, Liang G, Boily S, Van Neste A, Schulz R. Structural study and hydrogen sorption kinetics of ball-milled Mg hydride. J Alloy Comp 1999;293:495–500.
[25] Leiva DR, Floriano R, Huot J, Jorge AM, Bolfarini C, Kiminami CS, et al. Nanostructured MgH_2 prepared by cold rolling and cold forging. J Alloy Comp 2011;509S:444–8.
[26] Lang J, Huot J. A new approach to the processing of metal hydrides. J Alloy Comp 2011;509:L18–22.
[27] Huot J. Nanocrystalline metal hydrides obtained by severe plastic deformations. Metals 2012;2:22–40.
[28] Bazzanella N, Checchetto R, Miotello A. Atoms and nanoparticles of transition metals as catalysts for hydrogen desorption from magnesium hydride. J Nanomater 2011;2011:1–11.
[29] Klebanof L, Keller J. Final report for the DOE metal hydride center for excellence. 2012. SAND2012–0786.
[30] Guoxian L, Erde W, Shoushi F. Hydrogen absorption and desorption characteristics of mechanically milled Mg-35wt.% $FeTi_{1.2}$ powders. J Alloy Comp 1995;223:111–4.
[31] Vijay R, Sundaresan R, Maiya MP, Srinivasa Murthy S, Fu Y, Klein H-P, et al. Characterization of Mg–x wt.% FeTi (x = 5-30) and Mg-40 wt.% FeTiMn hydrogen absorbing materials prepared by mechanical alloying. J Alloy Comp 2004;384:283–95.
[32] Kondo T, Shindo K, Sakurai Y. Dependence of hydrogen storage characteristics of Mg-$TiFe_{0.92}Mn_{0.08}$ composite on amount of $TiFe_{0.92}Mn_{0.08}$. J Alloy Comp 2005;404–406:511–4.
[33] Varin RA, Zaranski Z, Czujko T, Polanski M, Wronski ZS. The composites of magnesium hydride and iron-titanium intermetallic. Int J Hydrogen Energy 2011;36:1177–83.
[34] Amirkhiz BS, Zahiri B, Kalisvaart P, Mitlin D. Synergy of elemental Fe and Ti promoting low temperature hydrogen sorption cycling of magnesium. Int J Hydrogen Energy 2011;36:6711–22.
[35] Chen B-H, Kuo C-H, Ku J-R, Yan P-S, Huang C-J, Jeng M-S, et al. Highly improved with hydrogen storage capacity and fast kinetics in Mg-based nanocomposites by CNTs. J Alloy Comp 2013;568:78–83.
[36] Leal Neto RM, Silva RA, Floriano R, Coutinho GCS, Falcão RB, Leiva DR, et al. Synthesis by high-energy ball milling of MgH_2-TiFe composites for hydrogen storage. Mater Sci Forum 2017;899:13–8.
[37] Falcão RB, Dammann EDCC, da Rocha CJ, Ichikawa RU, Durazzo M, Martinez LG, et al. Synthesis of TiFe compound from ball milled TiH_2 and Fe powders mixtures. Mater Sci Forum 2014;802:61–5.
[38] Keijser TH, Langford JI, Mittemeijer EJ, Vogels ABP. Use of the Voigt function in a single-line method for the analysis of X-ray diffraction line broadening. J Appl Crystallogr 1982;15:308–14.
[39] Keijser TH, Mittemeijer EJ, Rozendaal HCF. The Determination of crystallite-size and lattice-strain parameters in conjunction with the profile-refinement method for the determination of crystal structures. J Appl Crystallogr 1983;16:309–16.
[40] Stadelmann P. [Internet]. Java-EMS: JEMS. c. 2004. Available from: http://cimewww.epfl.ch/people/stadelmann/jemsWebSite/jems.html.
[41] Kondo T, Shindo K, Arakawa M, Sakurai Y. Microstructure and hydrogen absorption-desorption properties of Mg-$TiFe_{0.92}Mn_{0.08}$ composites prepared by wet mechanical milling. J Alloy Comp 2004;375(1–2):283–91.
[42] Lima GF, Garroni S, Baró MD, Suriñach S, Kiminami CS, Botta WJ, et al. 2Mg-Fe alloys processed by hot-extrusion: influence of processing temperature and the presence of MgO and MgH_2 on hydrogenation sorption properties. J Alloy Comp 2011;509(1):460–3.
[43] Mandal P, Srivastava ON. Hydrogenation behaviour of the new composite storage material Mg-x% TiFe. J Alloy Comp 1994;205(1–2):111–8.